



Highly sensitive and selective isoprene sensing performance of ZnO quantum dots for a breath analyzer

Yunji Park, Ran Yoo, Seung ryull Park, Jun Ho Lee, Hwaebong Jung, Hyun-Sook Lee*, Wooyoung Lee*

Department of Materials Science and Engineering, Yonsei University, 50 Yonsei-ro, Seodaemun-gu, Seoul, 03722, Republic of Korea



ARTICLE INFO

Keywords:

Gas sensor
ZnO
Nanoparticles
Quantum dots
Isoprene
Biomarker

ABSTRACT

We report the quantum-size effect on the sensing properties of ZnO nanoparticles for the detection of isoprene. For this purpose, two types of ZnO particles with different sizes, including nanoparticles (NPs, ~25 nm) and quantum dots (QDs, ~5 nm), were prepared by a wet chemical method. The ZnO QDs exhibited excellent sensing performance to 1 ppm isoprene compared to NPs. The maximum sensing response and response time were ~42 and 8 s at 350 °C for the QDs, while ~5.6 and 40 s at 500 °C for the NPs, respectively. The higher sensing response, rapid response, and lower optimal working temperature of the ZnO QDs can be attributed to an increase in oxygen vacancies, band gap, and specific surface area owing to the small size effect. Both ZnO NPs and QDs showed the lower limit of 0.01 ppm for detecting isoprene. It is noted that the sensing properties of ZnO QDs to 1 ppm isoprene are superior to previously reported isoprene sensors that are based on semiconducting metal oxides. Furthermore, we demonstrated that the low concentration (0.4–6.2 ppm) of isoprene can be selectively detected within ~83 s using a recently developed miniaturized gas chromatography integrated with the ZnO QD sensor.

1. Introduction

Disease diagnosis using breath analysis has been used since the Hippocrates era. Modern breath analysis has begun after 1971, when it was proven that human breath contains more than 200 different volatile organic compounds [1]. Various components, such as water vapor, acetone, ammonia, NO, CO, and H₂S, are found in exhaled breath of patients. Some of these components are closely related to disease, such as asthma, diabetes, kidney disorder, halitosis, and lung inflammations [2]. Respiratory analysis for isoprene can constitute another potentially useful biomarker for health and disease, and can be widely applied in non-invasive diagnostic and screening areas of modern medicine [3]. Isoprene is one of the most important biomarkers in human exhaled breath and is considered to be formed along the mevalonate pathway of cholesterol synthesis [4]. The amount of isoprene in exhaled breath can be an indication of synthesized cholesterol, and its concentration corresponds to the action of cholesterol, which produces enzymes in the human body [5].

Analysis of exhaled breath has been suggested as a convenient and safe supplement for blood and urine sampling. Indeed, it is a non-invasive and painless procedure, and does not require skilled medical

staff for sampling [6]. Generally, gas chromatography (GC) combined with flame ionization or a mass selective detector is widely utilized for accurate analysis of exhaled breath post-sampling and various pre-treatment steps, which include dehumidification, filtering, gas reforming, and preconcentration [7]. However, large time consumption for analysis and expensive/bulky instrumentation interfere with the immediate and cost-effective diagnosis of disease. In this respect, chemoresistive gas sensors based on nanostructured metal oxides are promising due to their low fabrication cost, simple applicability, and compact size that can be easily incorporated into portable breath samplers [8]. In fact, several reports induced chemoresistive sensors based on TiO₂ [9], Ti doped ZnO [8], (Pt,Pd,Au)-loaded SnO₂ NPs [10], Pt doped SnO₂ [11], and WO₃ [12] that have been explored for the detection of isoprene. Among them, ZnO constitutes an alternative promising material for gas sensors, due to its high thermal and chemical stabilities, abundance, and better sensing properties [13]. In diverse metal oxide gas sensors' cases, the performance of gas sensors has been improved by controlling the structure and morphologies of nanoparticles, nanowires, and nanoplatelets [14]. It was found that the size of nanoparticles strongly influences gas sensing performance. For the grain size effect, Xu et al. reported a sharp increase in SnO₂ sensor

* Corresponding authors.

E-mail addresses: h-slee@yonsei.ac.kr (H.-S. Lee), wooyoung@yonsei.ac.kr (W. Lee).

<https://doi.org/10.1016/j.snb.2019.03.118>

Received 18 December 2018; Received in revised form 25 March 2019; Accepted 26 March 2019

Available online 27 March 2019

0925-4005/ © 2019 Elsevier B.V. All rights reserved.

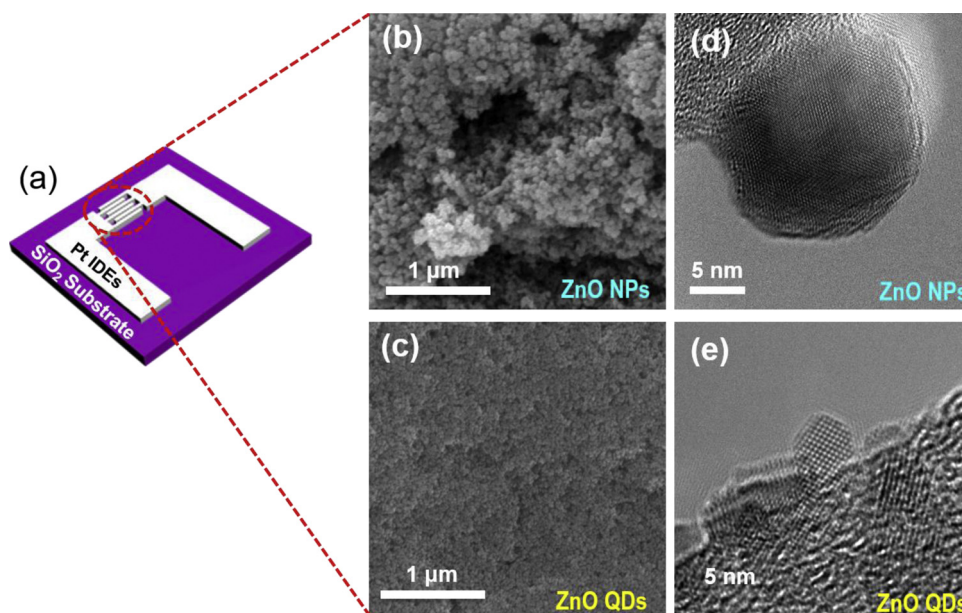


Fig. 1. (a) A schematic of a sensor device; (b), (c) SEM images of ZnO NPs and QDs dispersed on top of the interdigitated Pt electrodes after annealing, respectively; (d) and (e) TEM images of the filter-collected and isolated ZnO NPs and QDs, respectively.

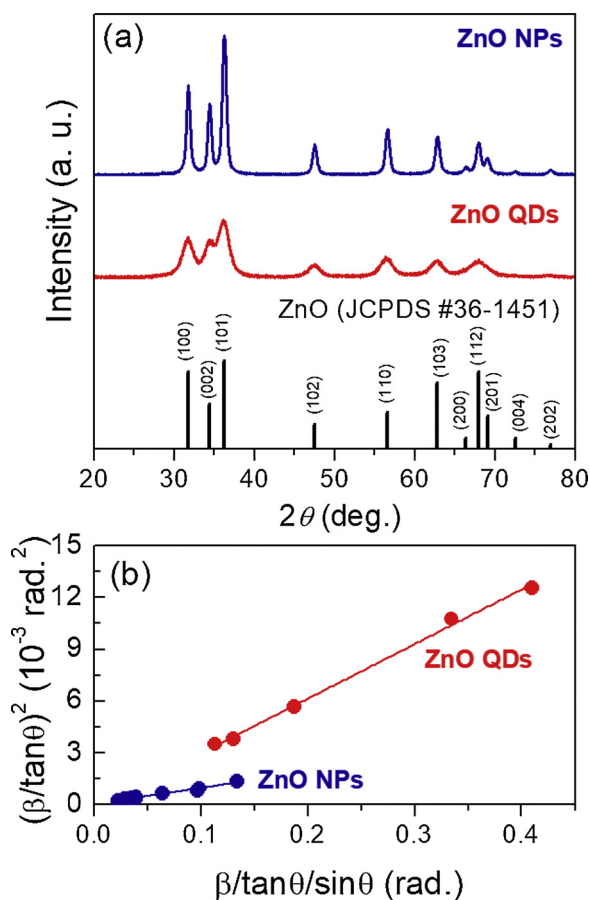


Fig. 2. (a) XRD patterns of ZnO NPs and QDs. The black bars at the bottom are for the reference and correspond to hexagonal wurtzite-type ZnO (JCPDS #36-1451); (b), (c) Halder-Wagner plots of ZnO NPs and QDs, respectively. Crystalline size is estimated from the y -intercept of the linear fit.

response as grain size decreased below 8 nm [15]. Thus, quantum-sized ZnO nanoparticles may facilitate new opportunities for gas sensing properties [16].

In a recent study, we developed a miniaturized gas chromatographic column (mini-GC) integrated with ZnO nanoparticles to detect acetone selectively from human breath [17]. By utilizing the manufactured mini-GC device incorporating a ZnO-based sensor, we could solve the selectivity problem of the target gas to other gases, which is possessed by most metal oxide-based semiconducting sensors. Furthermore, in a subsequent work, we found that the mini-GC device integrated with a ZnO nanoparticle-based sensor showed an excellent detecting ability of small amounts of chemical warfare agent simulants, particularly 2-chloroethyl ethyl sulfide (2-CEES), in a mixture of interfering gases, such as NH_3 , NO, and CO within 150 s [18]. Therefore, it is worth examining the selective detection of isoprene gas using the mini-GC integrated with quantum-sized ZnO nanoparticles.

In this work, we investigated the quantum-size effect on the gas sensing properties of ZnO nanoparticles for the detection of isoprene. We discuss the size effect of ZnO nanoparticles on the characteristics of oxygen vacancies, optical band gap, and specific surface areas that affect sensing performance. We tested the selectivity and sensitivity of the mini-GC incorporating quantum-sized ZnO nanoparticles to detect isoprene gas.

2. Materials and methods

2.1. Synthesis of ZnO NPs and QDs

ZnO nanoparticles (NPs) were synthesized by a hydrothermal method, as reported in our previous work [13]. The final NP samples were obtained by annealing at 350 °C for 30 min in an H_2/N_2 atmosphere. ZnO quantum dots (QDs) were synthesized by a wet-chemical method. We first prepared 0.1 M solution of zinc acetate dihydrate ($\text{Zn}(\text{CH}_3\text{COO})_2 \cdot 2\text{H}_2\text{O}$, Sigma Aldrich) dissolved in *N,N*-dimethylmethanamide ($\text{C}_3\text{H}_7\text{NO}$, DMF) and 0.3 M solution of tetramethylammonium hydroxide solution ($(\text{CH}_3)_4\text{NOH} \cdot 5\text{H}_2\text{O}$, TMAH, Sigma Aldrich) dissolved in methanol. The zinc precursor solution was mixed with the TMAH solution by stirring at 30 °C for 1 h. The suspended nanoparticles were collected by centrifuge, washed three times with acetone, and dispersed in methanol.

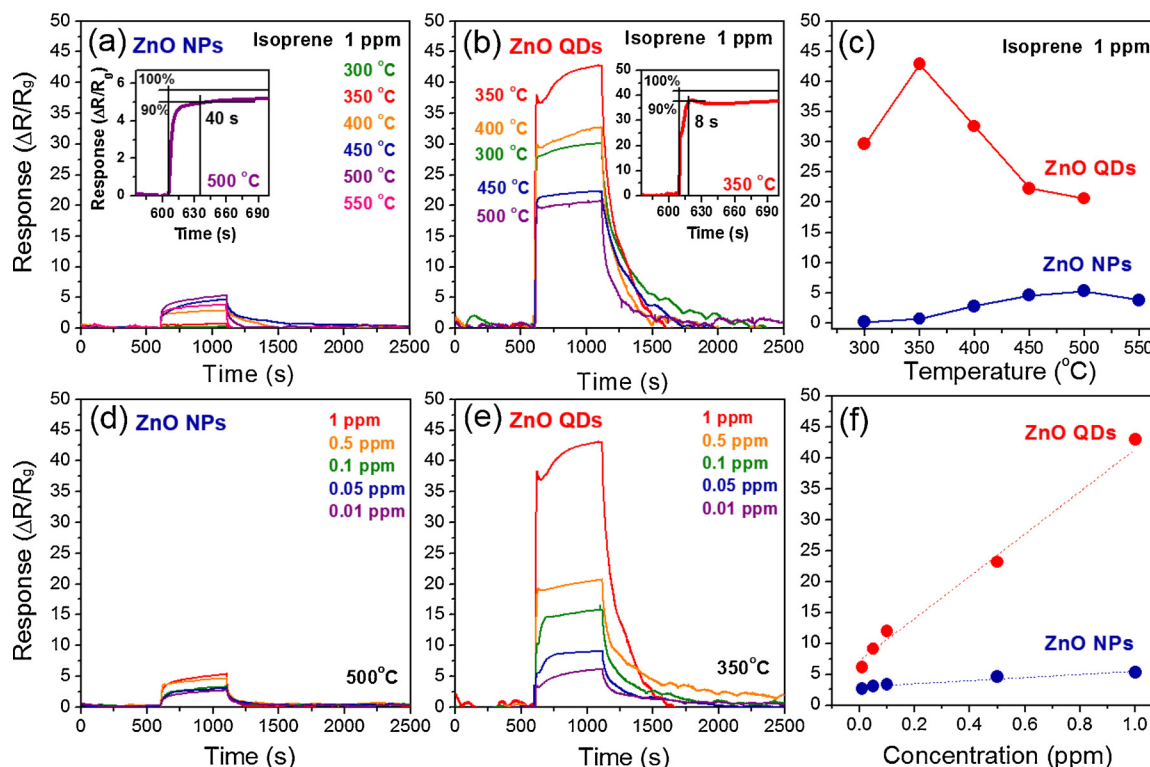


Fig. 3. (a), (b) Variation in the response of ZnO NPs and QDs to 1 ppm isoprene in the operating temperature range of 300–550 °C, respectively; (c) maximum sensing response of ZnO NPs (blue) and QDs (red) at 1 ppm isoprene as a function of operating temperature; (d) and (e) variation in the response of ZnO NPs and QDs at an optimum operating temperature as a function of isoprene concentration, respectively; (f) sensing response of ZnO NPs (blue) and QDs (red) to different concentrations of isoprene in the range of 0.01–1 ppm at their optimal working temperatures of 550 °C and 350 °C, respectively. Sensitivity was calculated from a slope with a linear fit of the response. (For interpretation of the references to colour in this figure legend, the reader is referred to the web version of this article).

2.2. Fabrication of sensor devices

The sensor device was prepared by fabricating Pt interdigitated electrodes on the patterned SiO₂ substrate. The Cr layer was used as an interlayer, which allows a good contact of Pt layer onto the SiO₂ substrate. The Cr and Pt layers were deposited with the thickness of 20 and 100 nm, respectively, on the SiO₂ substrate by a DC magnetic sputtering system. For the fabrication of ZnO NPs sensor, ZnO NPs mixed with α -terpineol binder was spread on the interdigitated Pt electrode. The sample of mixture was dried at 300 °C for 1 h and heated subsequently at 600 °C for 1 h. For the fabrication of the ZnO QD sensor, the ZnO QDs solution was dropped on the interdigitated Pt electrode. The sample were dried at 90 °C and subsequently annealed at 600 °C for 30 min. By these heating processes, the binding agent or solvent was removed, and sensor stability was improved.

2.3. Structural characterization

The morphology of the as-prepared ZnO NPs and ZnO QDs was investigated by field-emission scanning electron microscopy (FE-SEM, JEOL 7001 F) and transmission electron microscopy (TEM, JEOL JEM ARM 200 F). The crystal structure of ZnO NPs and ZnO QDs was characterized by X-ray diffraction (XRD, Ultima IV/ME 200DX, Rigaku) with Cu K α radiation. Surface elemental analysis was performed by X-ray photoelectron spectroscopy (XPS, K-alpha Thermo VG) with Al K α radiation (1486.6 eV). The specific surface area was estimated by BET (Brunauer-Emmett-Teller, BERTSOP-max) measurement, and the optical properties were examined using a UV-vis spectrophotometer (UV-vis, V650 JASCO) in the wavelength of 200–800 nm.

2.4. Gas sensing measurements

Sensing measurements were carried out in a chamber maintaining a flow system equipped with mass flow controllers (MFCs) and gas cylinders. The isoprene concentration was controlled in an air-balanced gas by adjusting the gas flow rates through MFCs. The sensing properties of the as-prepared ZnO NPs and QDs were examined using a unit of a current source (Keithley 6220) and a nanovoltmeter (Keithley 2182). For the measurements, a constant current of 10 nA was supplied for a time interval of 1 s. All of the gas sensing measurements were performed at operating temperatures of 300–550 °C. The sensing response for the isoprene gas is defined as $\Delta R/R_g$, where $\Delta R = (R_a - R_g)$. Here, R_g and R_a are the resistances of the sensor exposed to isoprene and plain air, respectively. The response time is defined as the time at which the resistance change upon exposure to the test gas reaches to 90% of total resistance. The recovery time is defined as the time at which the resistance change upon release of the test gas revert to 90% of the original resistance in a standard air condition.

3. Results and discussion

Fig. 1 shows the images of the sensor device and the as-synthesized ZnO particles. Fig. 1(a) presents a schematic image of the sensor device composed of interdigitated Pt electrodes on a Si/SiO₂ substrate with the size of 8.5 mm \times 8.5 mm. A periodic spacing of the interdigitated array of Pt electrodes is about 5 μ m. Figs. 1(b) and 1(c) show the SEM images of ZnO NPs and QDs spread on the electrode surface after annealing, respectively. Figs. 1(d) and 1(e) present high-resolution TEM images of the isolated ZnO NPs and QDs, respectively. The TEM images shown in Figs. 1(d) and 1(e) indicate that the ZnO NPs and QDs are spherical in shape and have a diameter of \sim 25 nm for NPs and \sim 5 nm for QDs.

The phase characterization of ZnO NPs and QDs was conducted by

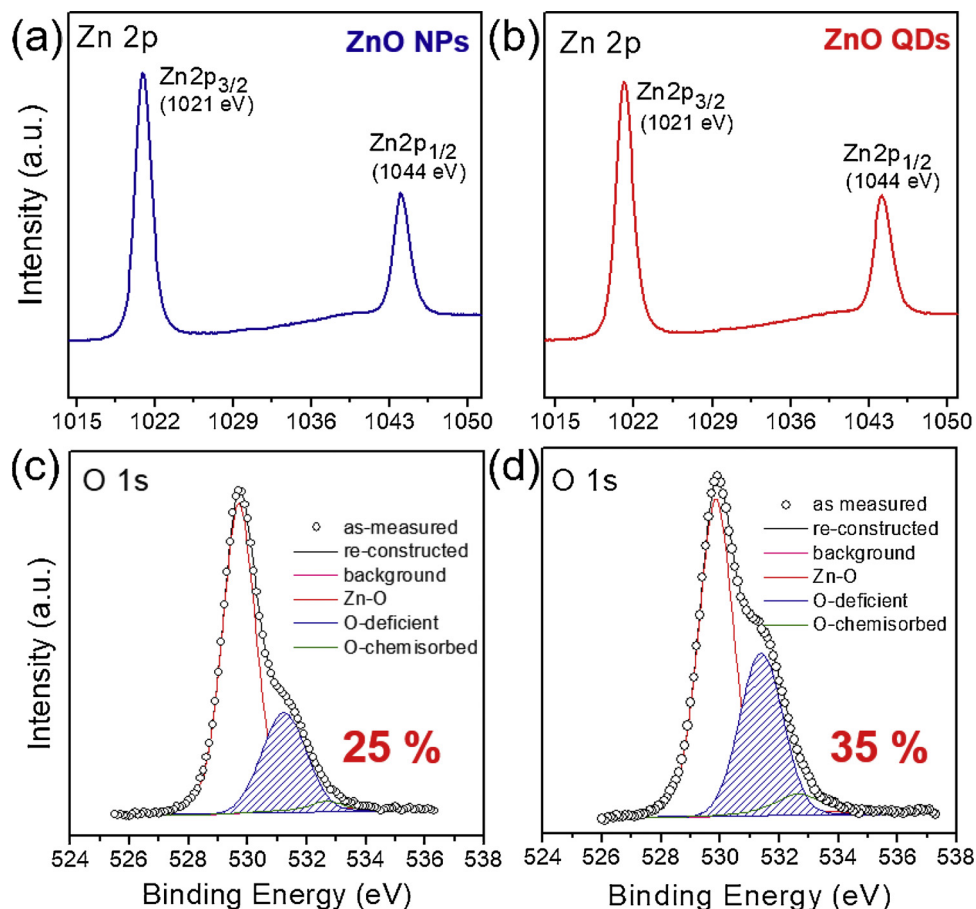


Fig. 4. XPS spectra of ZnO NPs and QDs for (a), (b) Zn 2p; (c), (d) O 1s, respectively.

XRD. Fig. 2(a) shows the XRD patterns of ZnO NPs and QDs, which are indexed to the crystal structure of a hexagonal wurtzite phase (JCPDS #36-1451). The result indicates that both ZnO NPs and QDs formed a hexagonal wurtzite structure without any secondary phase. As the crystallite size becomes smaller, the width of the diffraction peak becomes broader. We compared the crystallite size of the ZnO NPs and QDs using the Halder-Wagner method as follows (see Fig. 2(b)):

$$\left(\frac{\beta \cdot \cos\theta}{\sin\theta}\right)^2 = \frac{K\lambda}{D} \frac{\beta}{\tan\theta \cdot \sin\theta} + 16\epsilon^2 \quad (1)$$

where β is the integral breadth; K is the Scherrer constant, depending on the crystallite configuration; D is the crystallite size; λ is the wavelength of Cu K_{α} radiation; and ϵ is the weighted average strain [19]. By plotting $(\beta/\tan\theta)^2$ against $\beta/(\tan\theta \cdot \sin\theta)$, the y-intercept gives the mean value of the strain, and the slope gives the crystallite size [20]. When the K value of 4/3 for the mean volume-weighted size of spherical crystallites [21] is adopted, the crystallite size that was calculated using the Halder-Wagner method was ~ 20 nm for ZnO NPs and ~ 6.3 nm for ZnO QDs. These are in good agreement with the results obtained from the TEM analysis in Figs. 1(d) and 1(e).

The sensing properties of ZnO NPs and QDs were measured upon exposure to isoprene at different operating temperatures (300–550 °C) and concentrations (0.01–1 ppm). Figs. 3(a) and 3(b) present the variation in sensing responses of ZnO NPs and QDs to 1 ppm of isoprene at different operating temperatures. The maximum sensing response of the samples as a function of temperature was displayed in Fig. 3(c). As seen in Fig. 3(c), ZnO NPs and QDs exhibit a different response trend with respect to operating temperature. The highest sensing response to 1 ppm isoprene was observed to be ~ 42 at 350 °C for ZnO QDs and ~ 5.6 at 500 °C for ZnO NPs. Furthermore, the response time was estimated

from the response variation curve showing the highest sensing response in the inset of Figs. 3(a) and 3(b). This was approximately 8 s and 40 s for ZnO QDs and NPs, respectively. In comparison to ZnO NPs, ZnO QDs showed highly improved sensing performance, including significantly increased sensing response, much lowered optimal working temperature, and faster response time, under an exposure of 1 ppm isoprene.

Figs. 3(d) and 3(e) show the variation in sensing responses of ZnO NPs and QDs for different concentrations of isoprene, ranging from 0.01 to 1 ppm at their optimal working temperatures. The maximum sensing response of the samples as a function of isoprene concentration was presented in Fig. 3(f). With an increase in isoprene concentration, a linear increase of the response is observed in ZnO NPs and QDs. Moreover, Fig. 3(f) shows that ZnO NPs and QDs have a lower limit of 0.01 ppm to detect isoprene. The responses at 0.01 ppm isoprene were ~ 2.7 and ~ 6.1 , respectively. By a linear fitting, the sensitivities of the samples in the range of 0.01–1 ppm isoprene were estimated to be 2.5 and 35.5 for ZnO NPs and QDs, respectively. The linear correlation coefficient R^2 (0.93 for ZnO NPs and 0.99 for ZnO QDs) is close to 1, implying a good linearity. Thus, the sensor based on ZnO QDs exhibits significantly higher sensitivity compared to the ZnO NPs sensor.

In order to analyze the different sensing performances of ZnO NPs and QDs, we investigated the physical and chemical characteristics of sensing materials, including oxygen vacancies, band gap, and specific surface area. XPS analysis was performed to elucidate the chemical states of ZnO NPs and QDs. Fig. 4 presents the XPS spectra of Zn 2p and O 1s states for ZnO NPs and QDs. The Zn 2p spectra of ZnO NPs (Fig. 4(a)) and QDs (Fig. 4(b)) show two main peaks located at approximately 1021 eV and 1044 eV, indicating the electronic states of Zn 2p_{3/2} and Zn 2p_{1/2}, respectively. This indicates that a divalent oxidation state exists in ZnO NPs and QDs. Figs. 4(c) and 4(d) display the XPS

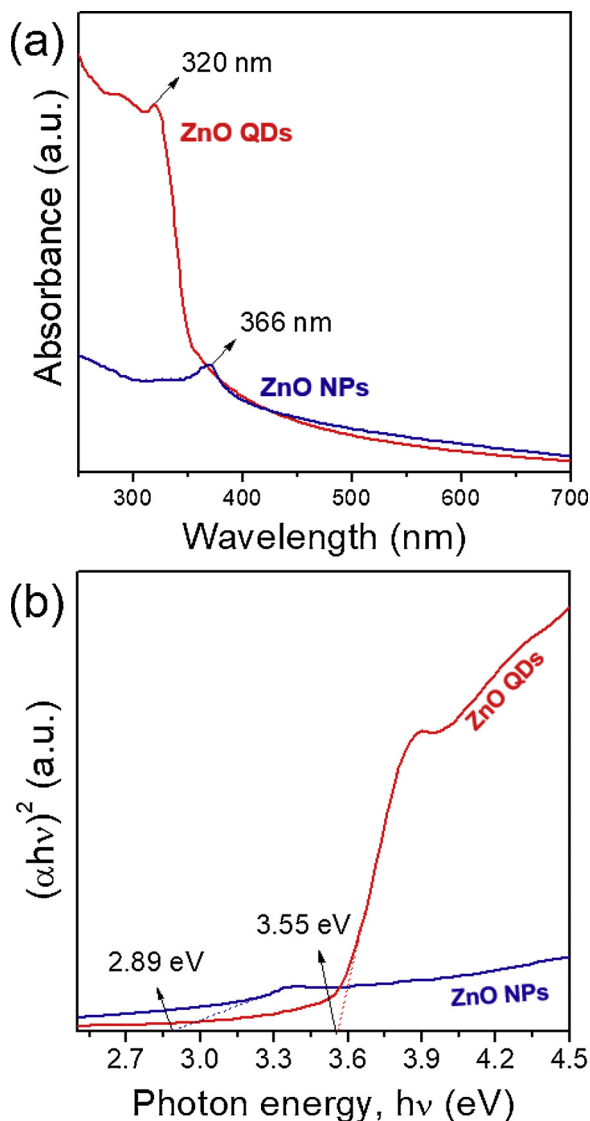


Fig. 5. (a) UV–vis absorption spectra and (b) optical band gap energies of ZnO NPs (blue) and QDs (red) (For interpretation of the references to colour in this figure legend, the reader is referred to the web version of this article).

spectra of O 1s state of ZnO NPs and QDs. The O 1s spectrum is fitted with three Gaussian peaks having three binding energy components. According to the literature [22], three peaks at 529.8 eV (red line), 531.2 eV (blue line), and 529.8 eV (green line) are associated with the O^{2-} ions of Zn–O bonding in the ZnO structure [23], the adsorbed oxygen ions of O^- and O^{2-} in the oxygen-deficient regions within the ZnO [24], and the chemisorbed oxygen species, such as the adsorbed O_2 , CO_2 , and H_2O on the surface of ZnO [24], respectively. Among those peaks, the second one is strongly related to the sensing performance because the peak intensity partly represents the amount of oxygen vacancies [24]. The amount of oxygen vacancies was evaluated by estimating the area fraction of the O-deficient peak in the deconvoluted O 1s peaks, as seen in Figs. 4(c) and 4(d). The percentages of oxygen vacancies were ~25% for ZnO NPs and ~35% for ZnO QDs. The results reveal that the ZnO QDs contain more oxygen vacancies than ZnO NPs, which leads to an enhancement in gas sensing properties in ZnO QDs. This is consistent to the close relationship between the concentration of oxygen vacancies and isoprene sensitivity of ZnO gas sensor observed in this work [25].

To further investigate the surface areas of ZnO NPs and QDs, N_2 adsorption-desorption analysis was conducted. The Brunauer-Emmett-

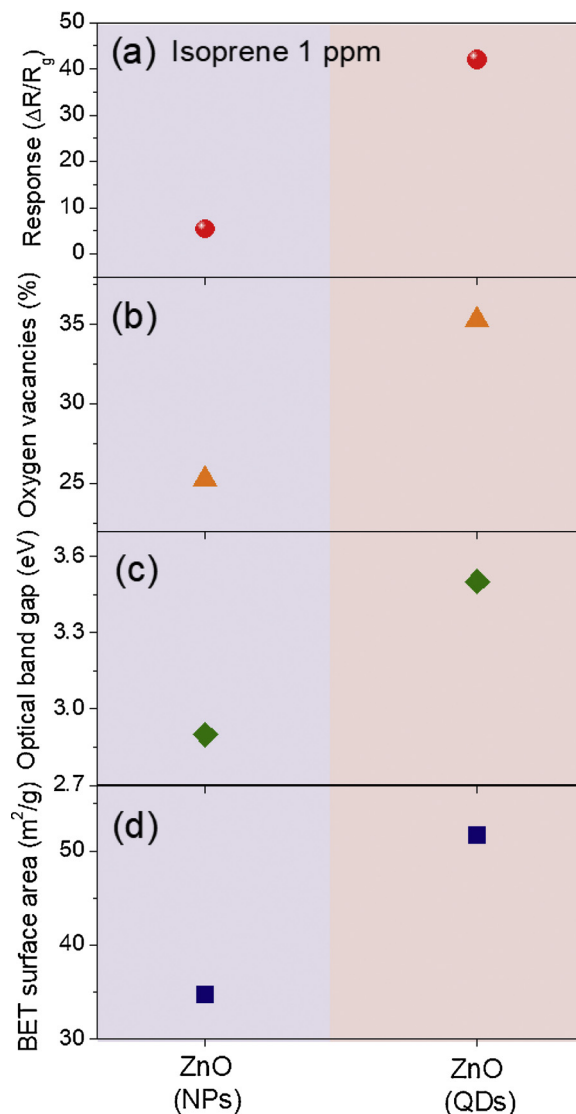


Fig. 6. Summary of the (a) sensing response, (b) oxygen vacancy, (c) optical band gap, and (d) BET surface area of ZnO NPs and QDs.

Teller (BET) specific surface areas of ZnO NPs and QDs were calculated from the N_2 adsorption branches. The BET surface areas of ZnO NPs and QDs are ~35 and ~51 m^2/g , respectively. The surface area of ZnO QDs is larger than that of ZnO NPs due to a volume reduction. Therefore, larger oxygen vacancies in ZnO QDs compared to ZnO NPs observed in Fig. 4 can be ascribed to the higher surface area of ZnO QDs.

The electronic structures of ZnO NPs and QDs were characterized by evaluating an optical band gap using UV–vis spectroscopy. Figs. 5(a) and 5(b) present the UV–vis absorbance spectra of the samples and the calculated band gap energy, respectively. In the absorption spectra (Fig. 5(a)), the peaks appear at ~366 nm for ZnO NPs and ~320 nm for ZnO QDs. It is clearly observed that the absorption peaks exhibited a blue shift with decreasing crystallite size of the ZnO particles due to the quantum confinement effect [26]. The optical band gap energy (E_g) can be evaluated using the Tauc equation as follows [27]:

$$\alpha h\nu = C(h\nu - E_g)^n \quad (2)$$

where E_g is the optical band gap; α is the absorption coefficient; $h\nu$ is the energy of the incident photons; C is a constant; and $n = 1/2$ for direct band-gap semiconductors. The optical band gap energy was calculated with extrapolation of the $[F(\alpha h\nu)^2]$ function versus $h\nu$ to zero [28]. The results are shown in Fig. 5(b). The optical band gaps of

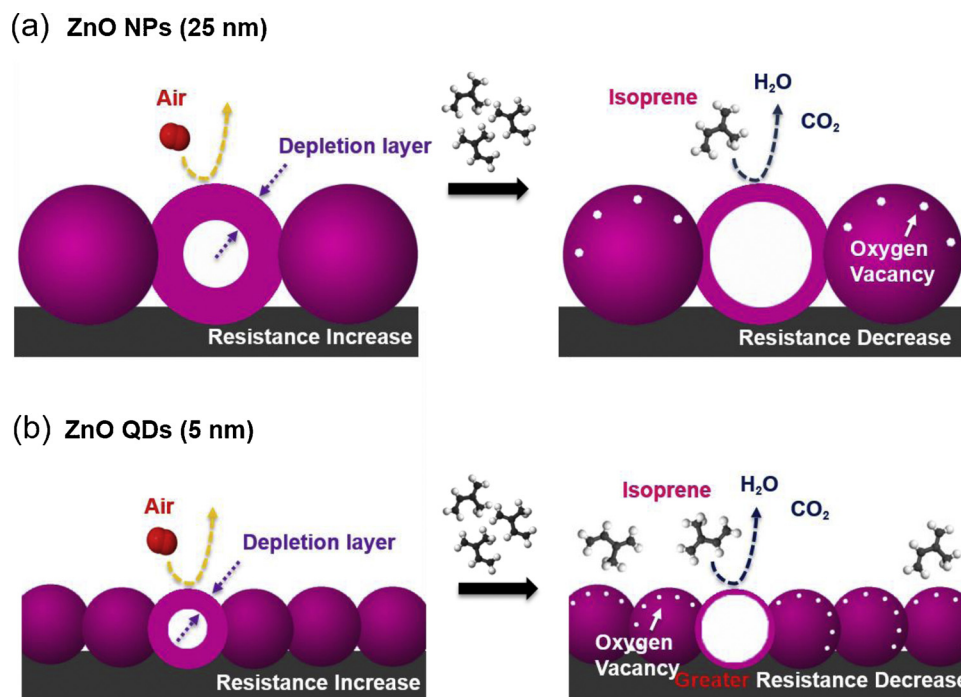


Fig. 7. A schematic of the sensing mechanism of (a) ZnO NPs and (b) ZnO QDs in air (left) and isoprene (right).

Table 1

Comparison of the isoprene sensing properties of various types of metal-oxide-based sensors.

Sensing materials	Operating temperature [°C]	Concentration [ppm]	Response (R_a/R_g)	Sensitivity* [ppm ⁻¹]	Detection limit [ppm]	Response time [s]	Ref.
ZnO QDs	350	1	42	~ 42.0	0.01	8	This work
ZnO NPs	500	1	5.6	~ 5.6	0.01	40	This work
TiO ₂ NPs	500	7.5	12	~ 1.6	1	130	[9]
Ti doped ZnO NPs	325	0.5	4.6	~ 9.2	0.005	60	[8]
Pt doped SnO ₂ NPs	400	0.5	3.3	~ 6.6	0.005	10	[11]
WO ₃ NPs	350	1	4.7	~ 4.7	0.2	20	[12]
(Pt,Pd,Au)-loaded SnO ₂ NPs	250	2.5	5.1	~ 2.0	0.1	60	[10]

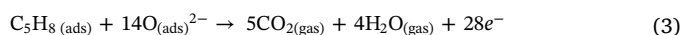
* sensitivity = response/concentration.

ZnO NPs and QDs are estimated to be 2.89 and 3.55 eV, respectively. According to the effective-mass model for spherical particles [29], the quantum confinement effect gives rise to band gap broadening, leading to the blue shift of the absorption peak in UV–vis. This result agrees well with the extant literature investigating many semiconductor nanostructures [30].

Fig. 6 presents the sensing response, oxygen deficiencies, optical band gaps, and specific surface areas of ZnO NPs and QDs. A remarkably enhanced response is observed in ZnO QDs as compared to NPs (see Fig. 6(a)). This can be attributed to the chemical and electronic synergistic effects due to an increase in oxygen vacancies (Fig. 6(b)), optical band gap (Fig. 6(c)), and specific surface area (Fig. 6(d)), arising from the influence of particle-size reduction. The augmented optical band gap in ZnO QDs due to the quantum confinement effect leads to a higher initial resistance of the sensor. Therefore, when the ZnO QDs sensor is exposed to the target gas of isoprene, ZnO QDs containing a greater number of oxygen vacancies or reactive sites undergo a considerable decrease in sensing resistance, resulting in a higher response of ZnO QDs.

From the above results, a possible mechanism for ZnO NPs and QDs in the detection of isoprene can be illustrated, as shown in Fig. 7. The electrical resistance of ZnO changes during the adsorption/desorption of gas molecules on the surface of ZnO. When ZnO NPs and QDs are exposed to air (see left in Figs. 7(a) and 7(b)), the adsorbed oxygen

molecules on the surface of ZnO NPs and QDs trap the electrons from the conduction band of ZnO, resulting in chemisorbed surface oxygen species (O_2^-) [31]. This produces a thick depletion layer on the ZnO surface, which increases the electrical resistance in ZnO NPs and QDs. When ZnO are exposed to isoprene (see right in Figs. 7(a) and 7(b)), a charge exchange occurs owing to the interaction between isoprene (C_5H_8) and the adsorbed oxygen species, leading to the oxidation of isoprene and the release of electrons back to the ZnO conduction band. At the working temperature of ZnO NPs and QDs ($T > 300^\circ\text{C}$), the O_2^- species mainly interact with isoprene molecules, according to the following equation:



Accordingly, a large number of electrons return back to the conduction band of ZnO, the thickness of the depletion layer is reduced. Therefore, the electrical resistance of ZnO NPs and QDs decreases. Both ZnO NPs and QDs possess the same mechanism mentioned above. However, ZnO QDs in air have a higher initial resistance due to a larger band gap, owing to the quantum confinement effect and more oxygen vacancies (i.e., reaction sites for isoprene) due to a higher surface-to-volume ratio. Therefore, the greater number of surface-sensing reactions of isoprene occurs in ZnO QDs upon exposure to isoprene, and this leads to the significant decrease in resistance (i.e., higher sensing response). Further, we compare the isoprene sensing performance of ZnO

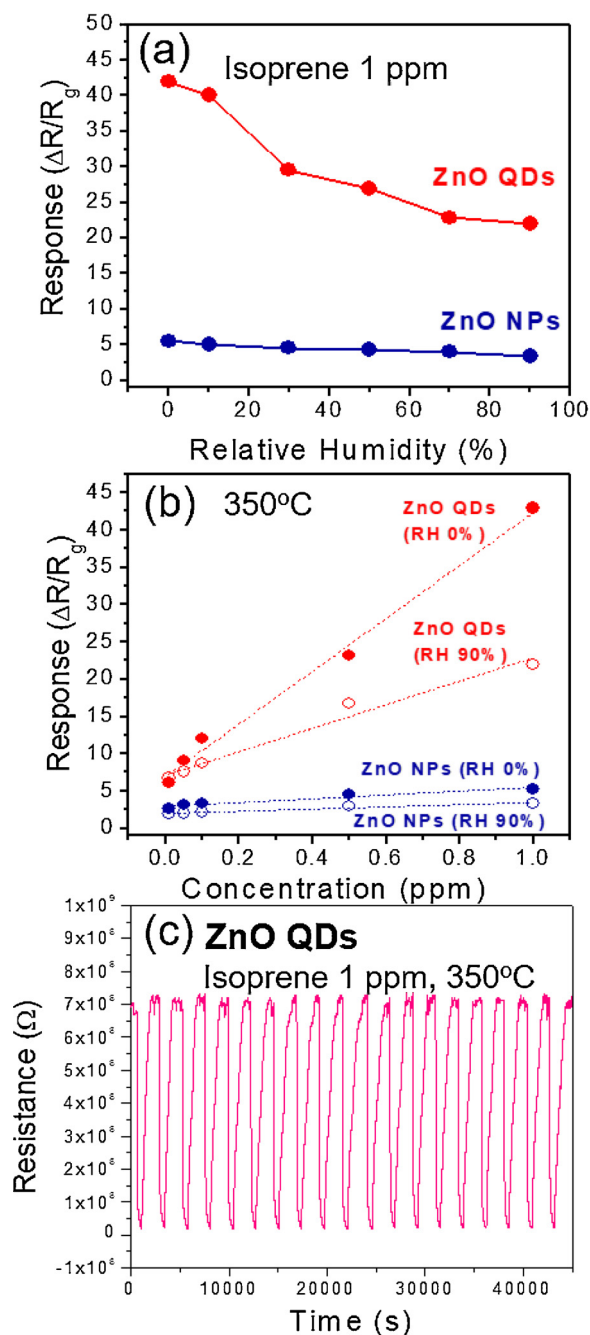


Fig. 8. (a) Variation in the sensing response of ZnO NPs (blue) and QDs (red) for 1 ppm isoprene as a function of relative humidity (RH) at the optimal operating temperature of 500 °C and 350 °C, respectively; (b) sensitivity of ZnO NPs (blue) and QDs (red) in the range of 0.01–1 ppm isoprene under conditions without humidity and with 90% RH; (c) Reproducibility of ZnO QDs in sensing 1 ppm isoprene over 20 cycles at 350 °C and (For interpretation of the references to colour in this figure legend, the reader is referred to the web version of this article).

NPs and QDs with those of previously reported metal-oxide based gas sensors [9–12,32] (see Table 1). It is obvious that ZnO QDs show a superior sensing response. This result infers that decreasing the particle size to a quantum-size is a promising way to improve sensing performance for isoprene.

For breath analyzer applications, providing only a low detection limit and high sensitivity is insufficient, but a high sensing response in a humid condition (~89–97 relative humidity (RH)%) is requisite [32]. Therefore, we tested the sensing properties of ZnO NPs and QDs in

various humid conditions. Fig. 8(a) presents the sensing response of the samples to 1 ppm of isoprene under different humid conditions (0–90 RH%) at their optimal working temperatures. As the relative humidity increases, the response decreases to ~22 for ZnO QDs and ~3.4 for ZnO NPs at 90 RH%. This indicates ~52% and ~61% reduction in response to 1 ppm of isoprene for ZnO QDs and NPs, respectively. This is attributed to contamination of reactive sites of ZnO by adsorption of water molecules. As seen in Fig. 8(b), sensitivity also decreases under the humid condition of 90 RH%: ~15.8 for ZnO QDs and ~1.5 for ZnO NPs. This can be inferred from the decrease in slope. However, a noteworthy feature is that ZnO NPs and QDs still have the lower detection limit of 0.01 ppm, even under a high humid condition. The reproducibility of the ZnO QDs based sensor under an exposure of 1 ppm isoprene were tested at its optimal operating temperature of 350 °C. Fig. 8(c) shows the reproducibility of ZnO QDs for sensing 1 ppm isoprene over 20 cycles at 350 °C. The sensing resistance is almost constant for 20 cycles of gas input and release, which implies good repeatability of the response of ZnO QDs for 1 ppm isoprene.

We tested the selective detection of isoprene gas using the mini-GC integrated with ZnO QDs. The manufacturing method of the mini-GC using ZnO QDs and sensing process of the mini-GC device are described in detail in our previous reports [17,18]. The response of the ZnO QDs sensor was defined as Δ Sensor signal, indicating the logarithmic difference in the sensor resistances in air and under target gases:

$$\Delta \text{ Sensor signal} = \log(\text{Resistance})_{\text{max}} - \log(\text{Resistance})_{\text{min}} \quad (4)$$

where $\log(\text{Resistance})_{\text{max}}$ denotes the maximum resistance before the sensor is exposed to the target gas; and $\log(\text{Resistance})_{\text{min}}$ is the minimum resistance during the exposure. Fig. 9 shows the sensing performance of the ZnO QDs sensor using the mini-GC device. Fig. 9(a) presents the sensor signal of the mini-GC integrated with the ZnO QDs sensor with time for air and air-based isoprene gases with various isoprene concentrations (0.4–25 ppm) at the optimal working temperature of 315 °C. Fig. 9(b) shows the Δ Sensor signal of the device for an isoprene concentration of 25 ppm at various operating temperatures. The maximum Δ Sensor signal was observed at 315 °C, implying the optimal operating temperature of the mini-GC device integrated with ZnO QDs. As shown in Fig. 9(a), the chromatograms of the air-based isoprene gases exhibit two peaks at ~34 s and ~83 s. The chromatograms of the gas with higher isoprene concentration of 12.5 and 25.0 ppm show a small peak at ~34 s and considerably large peak at ~83 s. However, the curves of gas with lower concentrations from 6.2 to 0.4 ppm exhibit a single peak at ~83 s. Thus, the peak at ~83 s and ~34 s corresponds to the detection of isoprene and some components of air (N_2), respectively. From this result, we confirmed that isoprene concentrations in the range of 0.4–6.2 ppm can be separately detected using the mini-GC integrated with ZnO QDs-based sensors. Fig. 9(c) presents the peak height of the Δ Sensor signal curves seen in Fig. 9(a) at various isoprene concentrations (0.4–25 ppm). The peak height can be defined as a sensing ability. As shown in Fig. 9(c), the response of the mini-GC integrated with the ZnO QDs sensor has a strong linear correlation with isoprene concentration ($R^2 = 0.982$). The detection limit of the device was found to be 0.04 ppm. Consequently, it is noted that the selective detection of isoprene gas is at the low concentration of 0.4–6.2 ppm. This is noteworthy because this is the first report to detect a small amount of isoprene gas with high selectivity and sensitivity.

4. Conclusion

We investigated the quantum-size effect on the sensing properties of ZnO particles synthesized using a wet chemical method for the detection of isoprene. Two types of ZnO particles, including nanoparticles (NPs) and quantum dots (QDs), with different sizes were prepared. TEM and XRD analyses revealed that the synthesized nanoparticles of ZnO NPs and QDs are spherical in shape and have a hexagonal wurtzite

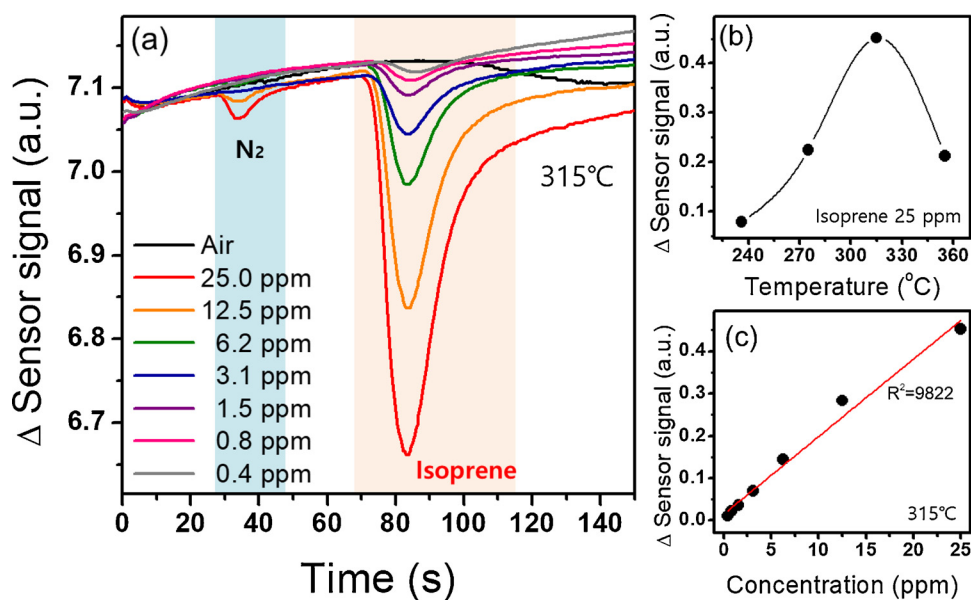


Fig. 9. (a) Δ Sensor signal changes of a miniaturized gas chromatographic column (mini-GC) integrated with the ZnO QDs sensor for various isoprene concentrations (0–25 ppm) at the optimal working temperature of 315 °C, (b) variation in Δ Sensor signal of the device for an isoprene concentration of 25 ppm at various operating temperatures, and (c) peak height of the Δ Sensor signal, corresponding to the response, at various isoprene concentrations (0.4–25 ppm) at 315 °C.

phase with a diameter of ~ 25 nm for NPs and ~ 5 nm for QDs. From the isoprene sensing test, we found that ZnO QDs exhibit better sensing performance than NPs for 1 ppm isoprene. The maximum sensing response and response time were ~ 42 and 8 s at 350 °C for the QDs, while ~ 5.6 and 40 s at 500 °C for the NPs, respectively. Through XPS, BET, and UV–vis measurements, we analyzed the size effect on the chemical and electronic properties of ZnO NPs and QDs, leading to reasons for their different sensing performance. Accordingly, the higher sensing response, rapid response, and lower optimal working temperature of ZnO QDs compared to NPs can be attributed to an increase in oxygen deficiencies, band gap, and surface area owing to the small size effect. Furthermore, we found that the sensing response of ZnO QDs to 1 ppm isoprene is superior to previously reported isoprene sensors that are based on semiconducting metal oxides. More importantly, we achieved the successful detection of low concentrations (0.4–6.2 ppm) of isoprene within ~ 83 s using the ZnO QD sensor incorporated in a miniaturized gas chromatography (mini-GC) that is recently developed by our group. This demonstrates that the mini-GC device integrated with the ZnO QDs can be utilized in breath isoprene analyzers to rapidly and accurately detect isoprene due to its high selectivity and sensitivity.

Acknowledgements

This research was supported by the Basic Science Research Program (2017M3A9F1052297) through the National Research Foundation of Korea (NRF), and the Medium and Large Complex Technology Commercialization Project (2019K000045) through the Commercialization Promotion Agency for R&D Outcomes. Both were funded by the Korea government (the Ministry of Science, ICT, and Future Planning).

References

- [1] S. Anil, Modak: single time point diagnostic breath tests: a review, *J. Breath Res.* 4 (2010) 017002.
- [2] Il-Doo Kim, How can nanotechnology be applied to sensors for breath analysis? *Nanomedicine* 12 (2017) 2695–2697.
- [3] R. Salerno-Kennedy, K.D. Cashman, Potential applications of breath isoprene as a biomarker in modern medicine: a concise overview, *Wien. Klin. Wochenschr.* 117 (2005) 180–186.
- [4] W. Miekisch, J.K. Schubert, G.F.E. Noeldge-Schomburg, Diagnostic potential of breath analysis—focus on volatile organic compounds, *Clin. Chim. Acta* 347 (2004) 25–39.
- [5] J.P. Spinhirne, J.A. Koziel, N.K. Chirase, A device for non-invasive on-site sampling of cattle breath with solid-phase microextraction, *Biosyst. Eng.* 84 (2003) 239–246.
- [6] J. King, H. Koc, K. Unterkofler, P. Mochalski, A. Kupferthaler, G. Teschl, S. Teschl, H. Hinterhuber, A. Amann, Physiological modeling of isoprene dynamics in exhaled breath, *J. Theor. Biol.* 267 (2010) 626–637.
- [7] J.W. Yoon, J.H. Lee, Toward breath analysis on a chip for disease diagnosis using semiconductor-based chemiresistors: recent progress and future perspectives, *Lab Chip* 17 (2017) 3537–3557.
- [8] A.T. Guntner, N.J. Pineau, D. Chie, F. Krumeich, S.E. Pratsinis, Selective sensing of isoprene by Ti-doped ZnO for breath diagnostics, *J. Mater. Chem. B Mater. Biol. Med.* 4 (2016) 5358–5366.
- [9] A. Teleki, S.E. Pratsinis, K. Kalyanasundaram, P.I. Gouma, Sensing of organic vapors by flame-made TiO₂ nanoparticles, *Sens. Actuators B Chem.* 119 (2006) 683–690.
- [10] T. Itoh, D. Lee, T. Goto, T. Akamatsu, N. Izu, W. Shin, T. Kasuga, S. Analysis of recovery time of Pt-, Pd-, and Au-Loaded SnO₂ sensor material with nonanal as large-molecular-weight volatile organic compounds, *Sens. Mater.* 28 (2016) 1165–1178.
- [11] J. van den Broek, A.T. Guntner, S.E. Pratsinis, Highly selective and rapid breath isoprene sensing enabled by activated alumina filter, *CS Sens.* 3 (2018) 677–683.
- [12] L. Wang, K. Kalyanasundaram, M. Stanacevic, P. Gouma, *Sens. Lett.* 8 (2010) 709–712.
- [13] R. Yoo, D.M. Lee, S.M. Cho, W.Y. Lee, *Sens. Actuators B Chem.* 254 (2018) 1242–1248.
- [14] M. Righettoni, A. Amann, S.E. Pratsinis, Breath analysis by nanostructured metal oxides as chemo-resistive gas sensors, *Mater. Today* 18 (2015) 163–171.
- [15] C. Xu, J. Tamaki, N. Miura, N. Yamazoe, Grain size effects on gas sensitivity of porous SnO₂-based elements, *Sens. Actuators B Chem.* 3 (1991) 147–155.
- [16] S. Bai, J. Hu, D. Li, R. Luo, A. Chen, C.C. Liu, Quantum-sized ZnO nanoparticles: synthesis, characterization and sensing properties for NO₂, *J. Mater. Chem.* 21 (2011) 12288–12294.
- [17] H. Jung, W. Cho, R. Yoo, H.-S. Lee, Y.-S. Choe, J.Y. Jeon, W. Lee, Highly selective real-time detection of breath acetone by using ZnO quantum dots with a miniaturized gas chromatographic column, *Sens. Actuators B Chem.* 274 (2018) 527–532.
- [18] J.H. Lee, H. Jung, R. Yoo, Y. Park, H.-S. Lee, Y.-S. Choe, W. Lee, Real-time selective detection of 2-chloroethyl ethyl sulfide (2-CEES) using an Al-doped ZnO quantum dot sensor coupled with a packed column for gas chromatography, *Sens. Actuators B: Chem.* (2018) – under review.
- [19] N.C. Halder, C.N.J. Wagner, Separation of particle size and lattice strain in integral breadth measurements, *Acta Cryst.* 20 (1966) 312–313.
- [20] S. Gopinath, J. Phillip, Preparation of metal oxide nanoparticles of different sizes and morphologies, their characterization using small angle X-ray scattering and study of thermal properties, *Mater. Chem. Phys.* 145 (2014) 213–221.
- [21] T. Ida, S. Shimazaki, H. Hibino, H. Toraya, Diffraction peak profiles from spherical crystallites with lognormal size distribution, *J. Appl. Crystallogr.* 36 (2003) 1107–1115.
- [22] J. Das, S.K. Pradhan, D.R. Sahu, D.K. Mishra, S.N. Sarangi, B.B. Nayak, S. Verma, B.K. Rout, Micro-Raman and XPS studies of pure ZnO ceramics, *Physica B* 405 (2010) 2492–2497.
- [23] M. Chen, X. Wang, Y.H. Yu, Z.L. Pei, X.D. Bai, C. Sun, R.F. Huang, L.S. Wen, X-ray photoelectron spectroscopy and auger electron spectroscopy studies of Al-doped ZnO films, *Appl. Surf. Sci.* 158 (2000) 134–140.
- [24] J. Wang, Y. Li, Y. Kong, J. Zhou, J. Wu, S. Wu, W. Qin, Z. Jiao, L. Jiang, Non-fluorinated superhydrophobic and micro/nano hierarchical Al doped ZnO film: the effect of Al doping on morphological and hydrophobic properties, *RSC Adv.* 5 (2015) 81024–81029.
- [25] M.W. Ahn, K.S. Park, J.H. Heo, J.G. Park, D.W. Kim, K.J. Choi, J.H. Lee, S.H. Hong, Gas sensing properties of defect-controlled ZnO-nanowire gas sensor, *Appl. Phys. Lett.* 93 (2008) 263103.

- [26] R.A. Gaashani, S. Radiman, A.R. Daud, N. Tabet, Y.A. Douri, XPS and optical studies of different morphologies of ZnO nanostructures prepared by microwave methods, *Ceram. Int.* 39 (2013) 2283–2292.
- [27] J. Tauc, *Amorphous and Liquid Semiconductors*, Plenum Press, New York, 1975, p. 171.
- [28] R.S. Weber, Effect of local structure on the UV-Visible absorption edges of molybdenum oxide clusters and supported molybdenum oxides, *J. Catal.* 151 (1995) 470–474.
- [29] L.E. Brus, Electron–electron and electron-hole interactions in small semiconductor crystallites: the size dependence of the lowest excited electronic state, *J. Chem. Phys.* 80 (1984) 4403.
- [30] R. Reisfeld, Nanosized semiconductor particles in glasses prepared by the sol–gel method: their optical properties and potential uses, *J. Alloys. Compd.* 341 (2002) 56–61.
- [31] J. Du, H. Yao, R. Zhao, H. Wang, Y. Xie, J. Li, Controllable synthesis of prism- and lamella-like ZnO and their gas sensing, *Mater. Lett.* 136 (2014) 427–430.
- [32] L. Ferrus, H. Guenard, G. Vardon, P. Varene, Respiratory water loss, *Respir. Physiol.* 39 (1980) 367–381.